Dynamic and Loaded Impedance Components in the Maintenance of Human Arm Posture

John M. Dolan, *Member, IEEE*, Mark B. Friedman, and Mark L. Nagurka, *Member, IEEE*

Abstract— **The postural stiffness of the human arm has previously been estimated by displacing the hand from a series of equilibrium positions and correlating the resultant displacements and restoring forces. We extend this experimental methodology to include measurement of dynamic components of impedance. The stiffness-damping-mass characteristics are represented numerically as matrices and graphically as ellipses characterized by size, shape, and orientation. The latter depict the predominant nonrotational component of the impedance force fields. The results suggest 1) joint damping is related to both joint stiffness and joint inertia, and 2) two-joint impedances, i.e., impedances associated with muscles connected across both the elbow and shoulder joints, play a relatively smaller role in damping than in stiffness. The ability to modulate stiffness in the face of initial static bias forces, i.e., "loading," is also examined. We observe regular shifts in the human arm endpoint's "spring center" corresponding to the bias force directions and magnitudes.**

I. Introduction

INVESTIGATIONS of human motor control have led to a wide variety of viewpoints concerning the strategy of the central nervous system (CNS) in controlling limb movements. Researchers have suggested control of muscle variables such as force, length, velocity, stiffness, and damping. The difficulty of positing a single strategy, in light of the vast complexity of the CNS and the great variety of tasks of which it is capable, has been well recognized [1]. Several researchers [2]–[6] have proposed the control of mechanical impedance as an important means of human motor control. Stiffness, damping, and mass are three basic components of mechanical impedance, relating force to position, velocity, and acceleration, respectively.

Theories and experiments regarding human limb impedance control have progressed historically from consideration of single muscles to the investigation of multi-jointed limbs. Feldman [2] showed that the (scalar) stiffness of an individual muscle about a fixed equilibrium length increases with neural activity. The coactivation of antagonist muscle pairs about a single joint allows the joint's equilibrium angle and its stiffness, or more generally its impedance, to be adjusted independently [5]. Muscle coactivation in a multijointed limb allows independent control of the mult-dimensional position and impedance of the limb endpoint. In the human arm, this control results from degrees of freedom provided by a combination of singly and doubly joint-connected antagonist muscle pairs at the shoulder and elbow [7]. Singly joint-connected muscle pairs connect a given joint to its adjoining limb link, whereas doubly joint-connected muscle pairs connect across two joints. Fig. 1 [5], [8] shows a simple human arm model combining singly and doubly joint-connected muscle pairs.

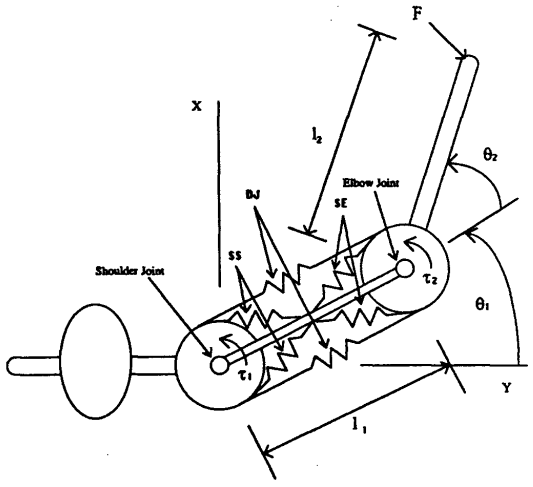

Fig. 1. Simple two-joint muscle model in the horizontal plane. SS are the singly connected shoulder muscles, SE the singly connected elbow muscles, and DJ the doubly connected muscles between the shoulder and elbow.

Several prior experiments related to multijoint impedance have been conducted. To investigate the way in which the CNS controls stiffness to achieve posture, Mussa-Ivaldi *et al.* [9] displaced the human arm endpoint from a series of positions in a horizontal plane and measured the corresponding restoring forces before the onset of any voluntary reaction. They concluded that the stiffness characteristic of the arm endpoint is "spring-like," in that it is symmetrical for small displacements about an equilibrium position. They characterized the stiffness of several human subjects at various positions using ellipses representing the loci of the restoring-force vectors. The orientation with respect to a frame fixed in the human shoulder and the shape, or aspect ratio, of these ellipses remained relatively constant among subjects, whereas their sizes varied.

In another multi-joint experiment, Flash [10] tested the equilibrium trajectory hypothesis (ETH) in an investigation of reaching motions. The ETH theorizes that the CNS temporally shifts the commanded limb equilibrium position in such a way that the muscular viscoelastic forces cause the limb to execute a desired trajectory. Flash used the following dynamic

Manuscript received January 9, 1992; revised November 20, 1992.

The authors are with the Robotics Institute, Carnegie Mellon University, Pittsburgh, PA 15213.

IEEE Log Number 9209629.

model of the human arm, relating joint torques τ to joint displacements Θ:

$$\tau = I(\Theta)\ddot{\Theta} + C(\Theta, \dot{\Theta}) \quad (1)$$

where $I(\Theta)$ is the human arm's inertia matrix, and $C(\Theta, \dot{\Theta})$ is a vector of centrifugal and Coriolis terms. The elbow and shoulder joint positions and their rates were measured during a movement and substituted in (1), resulting in the joint torques necessary to drive the arm. Under the assumption of the ETH, these torques were equated to a function of the joint velocities and of the instantaneous difference between the actual and equilibrium joint positions:

$$\tau = K(t)[\phi(t) - \Theta(t)] - B(t)\dot{\Theta}(t) \quad (2)$$

The unknowns in this function were the (voluntary) joint stiffness and damping matrices, $K(t)$ and $B(t)$, and the joint equilibrium positions $\phi(t)$. With no available experimental data on voluntary stiffness and damping, Flash assumed that postural damping scales with postural stiffness, which had been measured by Mussa-Ivaldi *et al.* [9], and that voluntary damping and stiffness scale with postural damping and stiffness, respectively. Flash observed that the calculated joint equilibria lay along nearly straight lines connecting the initial and target points, and concluded that the ETH is plausible.

Previous experimental measurements concentrated on the static component of impedance, i.e., stiffness, in the postural case. The studies reported here and by Dolan [11] in expanded form extend the measurement of human arm impedance to its dynamic components, damping and mass. In addition, whereas previous measurements of multi-joint stiffness have been made for the unloaded case [9], in which no significant forces act on the arm other than those which perturb it, the current work extends these measurements to the loaded case, in which the adaptation of the arm to environmental forces is considered.

II. Materials and Methods

Test Apparatus: A 2-DOF SCARA-configuration direct-drive robotic manipulator was constructed [12] and used to perturb the human arm endpoint in the horizontal plane. The manipulator arm was kinematically anthropomorphic, with upper arm and forearm link lengths of 0.30 m and 0.35 m, respectively. DC servo motors at each joint were current-controlled by an IBM PC AT. A Cartesian-error-based inverse-dynamics control approach was used to make the perturbation forces in various directions as uniform as possible. Position information was acquired from an 8000-count encoder on each joint, giving a spatial resolution of smaller than 0.25 mm throughout the manipulator workspace. An endpoint two-axis force sensor was designed for compactness, fitting within a comfortably graspable 54-mm-diameter handle. Each axis formed by a pair of strain gages in a parallelogram linkage, sensed forces of up to 44.5 N (10 lb) with a resolution of 0.011 N. The sensor had a mean dynamic high-frequency noise component of 0.05 N.

In the experimental setup, shown in Fig. 2, subjects were seated in front of the manipulator with their arms supported in the horizontal plane by a sling hanging from the ceiling

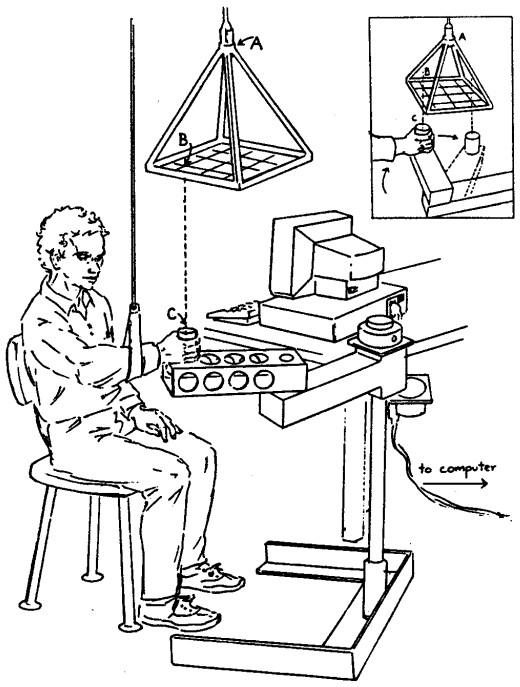

Fig. 2. Experimental Setup. The subject's arm remains in the horizontal plane. Desired positions are displayed to the subject by a light source at A, which projects the shadow of point B onto the top of the handle C.

about 3 m above the arm. Subjects grasped the force-sensor handle of the manipulator while receiving perturbations at five test positions. Following Mussa-Ivaldi *et al.* [9], who had measured the stiffness component under similar conditions, these positions are hereafter referred to as 1) reference, 2) distal, 3) proximal, 4) right, and 5) left. They were located at the following positions (mm) in a Cartesian frame centered at the subject's shoulder joint: 1) (0,380), 2) (0,520), 3) (0,240), 4) (295,380), 5) (−295,380). Visual targets for the positions were provided by a ceiling-mounted shadow-casting device. Data collection occurred on a software-interrupt basis at a sampling rate of 200 Hz.

Experimental Procedures: Both postural "unloaded" and "loaded" measurements of human arm impedance were conducted. In the postural unloaded experiment, subjects centered the force-handle on a 1-cm-diameter circular shadow marking a given position, and attempted to maintain posture in the face of a series of perturbations. Negligible forces acted on the arm in the plane prior to the onset of a perturbation. In order to limit conscious, voluntary response to perturbations, subjects were asked to not consciously attempt to re-center the handle on the shadow until the manipulator had stopped pushing against the arm. Several underdamped, rapidly rising ($t_r = 0.2\ s$) position perturbations were successively applied. Perturbations typically lasted 1.5-2.0 s. The interval between re-centering and the next perturbation was between 3 and 5

s, so that the perturbation onset was not easily predictable by the subjects. The imposed trajectories caused arm endpoint oscillations with maximum velocities and accelerations of approximately 0.8 m/s and 1.5 m/s^2, respectively. A typical set of position and force traces for a single perturbation is shown in Fig. 3. In order to avoid artifacts arising from varying manipulator configurations, different test positions were achieved by repositioning the subject's shoulder, rather than the manipulator. At a given test position, perturbations were issued in eight Cartesian directions obtained by aligning the first direction with the x-axis of the subject's shoulder frame and spacing each of the remaining seven at 45 *deg*. Eight perturbations thus described a full set by sampling impedance in a circle about the equilibrium point. Two full perturbation sets were issued at each test position. The commanded size of the perturbations was 5 mm, and excursions from the equilibrium point ranged as high as 10 mm during the dynamic phase of the motion. In order to limit an experimental subject's anticipation of an imminent perturbation, the experimenter typed on the keyboard continuously, using one key to initiate and another to terminate the perturbation. The experiment was administered to ten male subjects and one female subject between the ages of 22 and 45, with an average age of 29.5 years, and a standard deviation of 8.1 years.

In the postural loaded experiments, a bias force between 0.7 N and 1.0 N was slowly applied (over 2–3 s) to the arm endpoint prior to the onset of each perturbation. Once the bias force had been maintained to within a specified threshold for one second, a perturbation like that described in the postural unloaded experiment was applied. At each position, six sets of 16 perturbations were applied. The first and last sets used a bias force of zero and thus measured the postural unloaded impedance, which served as a basis for comparison. Sets two through five applied bias forces in the four directions corresponding to the major and minor axes of the subject's postural unloaded stiffness ellipse at the current position. The loaded experiment was administered to three subjects at the proximal, reference, and distal positions.

Data Analysis and Processing: The joint-based dynamics of the human arm were propagated out to the human arm endpoint in the horizontal plane (see the Appendix), yielding the 2-D Cartesian equation

$$F = M\ddot{X} + B\dot{X} + K(X - X_0) \tag{3}$$

where F is the force applied to the arm endpoint, X is the resulting displacement, and M, B, and K are the Cartesian impedance matrices of mass, damping, and stiffness matrices at equilibrium position X_0. The identification problem involved determination of M, B, K, and X_0 by fitting displacement X and its derivatives to the force F.

The data stored were the encoder trajectories for both manipulator joints and the force sensor voltage histories for both axes. These data were processed in two steps: 1) conversion to appropriate units, and 2) filtering. In the conversion step, encoder trajectories were translated into the Cartesian motions (m) of the manipulator/human arm endpoint in the subject's shoulder frame. Force sensor voltages were converted into manipulator endpoint forces (N) and resolved into the subject's shoulder frame, yielding F in (3).

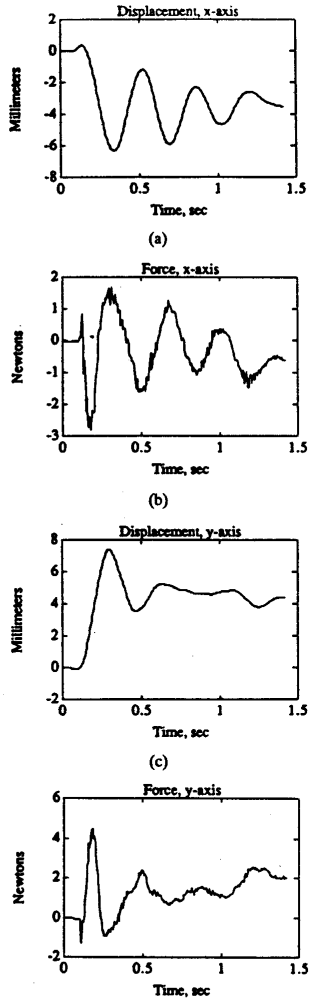

Fig. 3. Typical force and position trajectories for a single disturbance.

The force data resulted from an analog sensor, and were not filtered. The displacement signals stemmed from encoders with a resolution of 8000 ticks per revolution, resulting in a worst-case Cartesian resolution of 0.25 mm at the manipulator endpoint. The noise resulting from this uncertainty was non-Gaussian and had biasing effects on the identification results. Therefore, the x- and y-displacements of the endpoint were filtered forward and backward, to prevent phase shifts, using a second-order digital Butterworth lowpass filter with a cutoff frequency of between 7 and 10 Hz, and yielding X in (3). Estimates of the displacement-signal derivatives were obtained in three different ways: low-pass filtering followed by

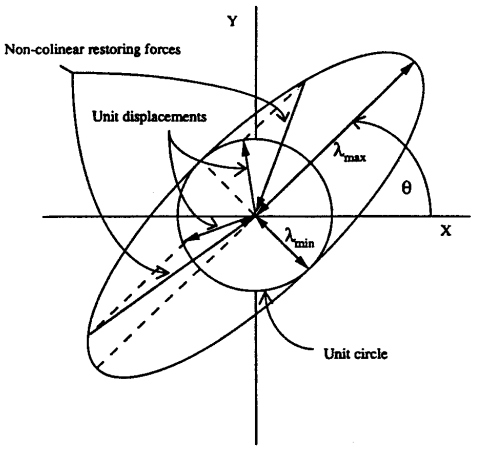

Fig. 4. Ellipse representation of impedance. The perimeter of the ellipse represents the locus of restoring force vectors for a unit displacement at various orientations. The displacement and restoring force are colinear only along the major and minor axes.

differencing [13], optimal frequency-domain filtering [14], and state-variable filtering [15]. Each of these led to a somewhat different estimate for the identified matrices in (3). The state-variable method yielded the most accurate results [11].

Data Representation: The identified matrices represent the relationship between a force vector and a displacement vector, or one of its time derivatives, and are thus descriptive of force fields. Each two-dimensional impedance matrix may be written generally as

$$Z = \begin{bmatrix} z_{11} & z_{12} \\ z_{21} & z_{22} \end{bmatrix} \tag{4}$$

and may be decomposed into symmetric, Z_s, and antisymmetric, Z_a, parts:

$$Z_s = \frac{1}{2}(Z + Z^T) \tag{5a}$$

$$Z_a = \frac{1}{2}(Z - Z^T). \tag{5b}$$

A concise graphical means of representing the symmetric component of such a matrix is as an ellipse (see Fig. 4) whose contour is the locus of force vectors produced by rotating a fixed-length displacement vector (or one of its derivatives, for the dynamic impedance components) about the origin [9]. Such an ellipse is characterized by size, shape, and orientation. The size is proportional to the determinant, the shape is given by the ratio of the larger to the smaller eigenvalue, and the orientation by the angle made by the principal eigenvector with the x-axis. The larger and smaller eigenvalues are equal to the forces exerted along the major and minor axes, respectively, against a rotated *unit* displacement. If the eigenvalues are not equal to one another, *i.e.*, if the contour is not a circle, it is only along these axes that the force is colinear with the displacement. For all other directions, the restoring force direction is determined as shown in Fig. 4.

The following equations transform the elements of the symmetric two-dimensional matrix

$$Z_s = \begin{bmatrix} s_1 & s_2 \\ s_2 & s_3 \end{bmatrix} \tag{6}$$

into size, shape, and orientation values:

$$\lambda_{2,1} = \frac{1}{2}[(s_1 + s_3) \pm \sqrt{(s_1 + s_3)^2 + 4(s_2^2 - s_1 s_3)}] \tag{7a}$$

$$A = \pi \lambda_1 \lambda_2 \tag{7b}$$

$$R = \frac{\lambda_2}{\lambda_1} \tag{7c}$$

$$\theta = \tan^{-1} \frac{\lambda_2 - s_1}{s_2} = \tan^{-1} \frac{s_2}{\lambda_2 - s_3} \tag{7d}$$

where λ_i are the eigenvalues ($\lambda_2 \geq \lambda_1$), and A, R, and θ are the size (area), shape (aspect ratio), and orientation values, respectively.

III. Results

Postural Unloaded Impedance: Identification of the mass, damping, and stiffness matrices in (3) was carried out using the three filtering methods. For each filtering method, all of the trajectories for a given test position were considered simultaneously from the onset of the perturbation to a specified end time in a recursive least-squares fit of the parameters. The parameter estimates for all three filtering methods converged to near-constant values within 0.5 *s*, remaining within 8% of these values until the selected end time of 1.0 *s*.

The extent of agreement between the filtering methods was determined by comparing their mass estimates, which were most subject to error from the filtering process due to their dependence on acceleration. In addition, the mass estimates could be compared to mass values obtained from a passive inertial model of the human arm. A similar check could not be made for the damping and stiffness, which result from neuromuscular inputs to the arm.

Unlike the optimal frequency-domain filter, in which optimal filter coefficients are automatically chosen for each trajectory, the lowpass and state-variable filters required tuning. The lowpass filter cutoff frequency was set at 10 Hz, and a second-order state-variable filter [15] of the form

$$T(s) = \frac{\omega_n^2}{s^2 + 2\zeta\omega_n s + \omega_n^2} \tag{8}$$

was chosen with its natural frequency ω_n tuned to the average peak frequency in the Fourier transform of the displacement data. The damping ratio ζ was set to a value close to that exhibited by the displacement data, approximately 0.1. With the exception of the mass values for the proximal position, the estimates for mass, damping, and stiffness given by the three filtering methods agreed with one another to within 15% of the maximum values in their respective matrices. The mass values at the proximal position differed from one another by as much as 25%, although the damping and stiffness values remained within 10% of one another.

In order to check the agreement of the mass matrices identified by the three filtering methods with the assumption

TABLE I
IMPLIED LINK MASSES m_1 AND m_2(kg) FOR THREE HUMAN SUBJECTS

Subject	Link masses	Filtering Method		
		Lowpass	Optimal	State-Variable
1	m_1	1.80±0.45	1.74±0.38	2.47±0.36
	m_2	1.56±0.13	1.49±0.11	1.54±0.10
2	m_1	1.58±0.69	1.61±0.47	2.19±0.53
	m_2	1.74±0.20	1.74±0.13	1.58±0.15
3	m_1	0.92±0.47	1.08±0.85	1.36 ±0.61
	m_2	1.36±0.13	1.28±0.24	1.23±0.17

of solely passive inertial effects, the inertia matrix $I(\Theta)$ was derived by modelling the upper arm and forearm as two cylindrical links in the horizontal plane with lengths l_1 and l_2, and masses m_1 and m_2, respectively. The link lengths were fixed based on anatomical measurements, and least-squares error minimization was used to determine the link masses implied by the Cartesian mass matrices identified at the five test positions. Data from the proximal position were found to skew the results and were therefore left out of the data set. The resulting implied link mass values, along with a single standard deviation, are given for three subjects in Table I.

The methods were consistent in their estimates of the forearm link mass, m_2, differing from one another by less than 10%. However, the variation among filtering methods in the estimates of the upper arm link mass m_1 was much higher. This was attributed to the fact that the forearm link was immediately excited by the manipulator, whereas the upper arm link was excited intermediately, by virtue of its connection to the forearm. Thus, the greatest information about the upper arm link mass was provided when the forearm was excited longitudinally. However, because it was in this direction that human arm damping was generally greatest, the excitation was not as persistent, and the resulting implicit upper arm mass estimates were less reliable. This problem appears to have been most severe at the proximal position, where the longitudinal damping was greatest among the positions, and the angular displacements, velocities, and accelerations of the upper arm were smallest.

In each case, the state-variable filtering method had the smallest ratio of standard deviation to estimated value for the upper arm mass. The process may be inverted to yield the Cartesian mass matrices corresponding to a given pair of implied link masses, and these mass matrices may be compared graphically to those experimentally identified. This is shown for the state-variable estimates for a typical subject in Fig. 5, and it is seen that the general character of the mass ellipses is captured by the assumption of passive inertial effects, with the largest deviations at the proximal position.

Damping and stiffness estimates for the three filtering methods were also compared. For all subjects, the maximum difference between corresponding individual damping matrix values for the three filtering methods was less than 15% of the maximum value in the compared matrices. For the stiffness values, this deviation was less than 10% at all positions.

In order to examine the degree of stability of the damping matrix estimates with respect to changes in the mass matrix estimates, a constrained identification was carried out. The

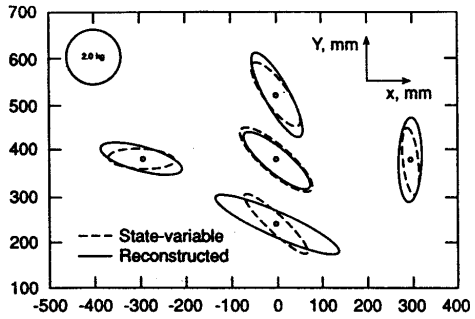

Fig. 5. Identified and modeled mass ellipses, subject 1. The radius of the calibration circle in the upper left-hand corner corresponds to 2.0 kg. The dashed-line ellipses are those directly identified by experiment. The solid-line ellipses are those found by least-squares fitting the experimental data to a two-cylindrical-link passive model of the human arm.

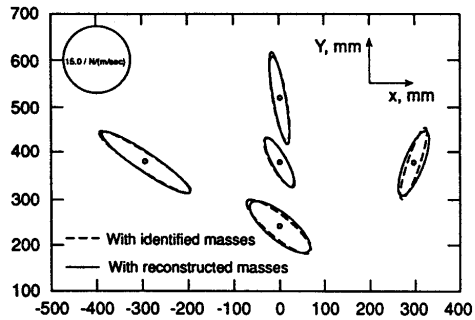

Fig. 6. Damping for identified and modeled masses, subject 1. The radius of the calibration circle corresponds to 15.0 N m/s. The damping ellipses corresponding to the two cases for the mass ellipses shown in Fig. 5 are shown here. The dashed-line ellipses result from an "unconstrained" identification. The solid-line ellipses result when the mass ellipses are constrained to be the modeled, or reconstructed, masses of Fig. 5.

mass estimates were set equal to those reconstructed by the implied human arm link masses found above, and the stiffnesses were set equal to those found in the unconstrained identification. The resulting damping values differed by less than 5% of the maximum values of their respective matrices. The changes in size, shape, and orientation of the damping estimates were also small. Thus, the damping estimates remain rather stable even when the mass estimates are adjusted to conform to the assumption of solely passive effects. Fig. 6 illustrates this stability by showing the damping ellipses for a single subject in the constrained and unconstrained cases.

In summary, the mass, damping, and stiffness matrix estimates from the three filtering methods were found to be largely mutually confirmatory. However, the state-variable method gave mass estimates which conformed most closely to those expected from a passive model of the human arm inertia matrix. The state-variable estimates were therefore used as the basis for further analysis.

Antisymmetric Impedance Component: The magnitudes of the antisymmetric components of the identified impedance matrices were measured in order to determine the magnitude

of the purely rotational force field, or curl. In the cases of mass and stiffness, the size of the rotational component is a measure of the conservative nature of the impedance with respect to energy. Because damping forces are strictly dissipative, zero curl in the case of damping does not have the interpretation of conservativity. However, Hogan [7] has argued that for both damping and stiffness, the only way to produce non-zero curl is through intermuscular feedback with unequal gains. The zero-curl component of the impedance is therefore due to some combination of intrinsic muscle properties and intermuscular feedback with equal gains.

Two straightforward normalized measures of the magnitude of the antisymmetry of a matrix are given by the ratios of its skew-symmetric component to its maximum and minimum eigenvalues ($p_{\min} = z_a/\lambda_{\max}$ and $p_{\max} = z_a/\lambda_{\min}$). These measures give the percentage rotational force with respect to the forces along the major and minor impedance ellipse axes. A single, combined measure is given by the geometric mean of $p_{\min}$ and $p_{\max}$

$$p_{\text{mean}} = \sqrt{p_{\min} p_{\max}} \tag{9}$$

and may be regarded as a percentage curl, or percentage rotational force field [9].

In the stiffness case, the findings of Mussa-Ivaldi *et al.* [9] were confirmed. For seven of the eleven subjects, p_{mean} was less than 15% for all stiffness matrices. One subject had anomalously high values for p_{mean} at positions one through four (41, 27, 32, and 18%). Neglecting these anomalous values, p_{mean} was 25% or less in all cases, 15% or less in over 90% of the cases, and 10% or less in 80% of the cases. As reported previously [9], these generally small percentage-curl values suggest that human arm stiffness is primarily spring-like, or conservative. In the case of mass, p_{mean} was 25% or less in all cases, and 15% or less for 95% of the matrices. These small percentage curl values imply the conservative nature of the human arm mass characteristic. In the case of damping, p_{mean} was again relatively small, being 25% or less for all matrices, and 15% or less for 75% of the matrices. The predominant, symmetric component of the impedance matrices, which can be graphically represented by an ellipse giving a locus of restoring-force vectors, is considered in the following sections.

Patterns of Impedance: Certain patterns in the orientation, size, and shape characteristics of the impedance ellipses were observed for single subjects and among subjects. The orientation of the impedance ellipses remained fairly consistent among subjects. The maximum standard deviation of the orientation angle across all positions, subjects, and ellipse types (mass, damping, and stiffness) was 11 *deg*. As the distance of the arm endpoint from the shoulder frame increased, the orientation angle of the impedance ellipses tended to increase in a clockwise direction. For all subjects, the stiffness ellipses were rotated clockwise with respect to the mass ellipses at all positions. The angle of this rotation for a given subject was roughly constant, and its average value ranged among subjects from 22 to 39 *deg*. About two-thirds of the damping ellipses were rotated by more than 5 *deg* with respect to their corresponding stiffness ellipses. The orientation of the mass, damping, and stiffness ellipses gave a "fan effect" in most

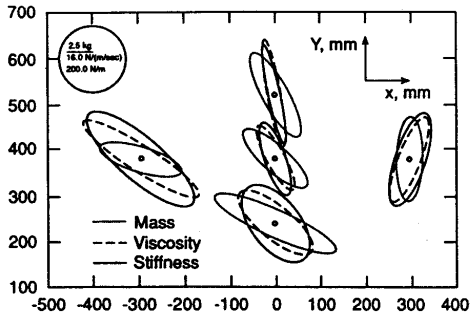

Fig. 7. Mass, damping, and stiffness ellipses, subject 2. The radius of the calibration circle corresponds to 2.5 kg, 16.0 N m/s, and 200.0 N/m for the mass, damping, and stiffness ellipses, respectively.

cases, with the damping ellipse oriented in more than 80% of the cases somewhere between the mass and stiffness ellipses. Although there were in most cases significant differences in orientation between the damping and stiffness ellipses, the damping ellipse orientations were generally closer to those of the stiffness ellipses than to those of the mass ellipses. Fig. 7 shows the mass, damping, and stiffness ellipses for a typical subject, illustrating the general characteristics described.

The shape of the stiffness ellipses for a given subject followed a regular pattern. At the proximal position, the stiffnesses were most nearly circular, ranging in shape from 1.3 to 3.2. As the arm endpoint moved further away from the body, the stiffnesses generally become more elongated, reaching maximum shapes of as high as 8.3 at the distal position. Among subjects, shapes at a given position varied by as much as a factor of 3.3. Contrary to the conclusion reached by Mussa-Ivaldi *et al.*[9], this demonstrates a significant difference in the shape characteristic of stiffnesses among subjects. Damping shapes also tended to increase as the arm endpoint distance from the body increased, but damping shape varied among positions to a smaller degree than did the stiffness shape.

Model Validation: For the human arm at rest, M in (3) arises from the passive inertial behavior of the arm, whereas K results from coactivation of opposing, or antagonist, muscle groups. The velocity-related term in a given model for the arm's endpoint behavior could conceivably stem from the inertial and kinematic character of the arm, in the form of Coriolis and centrifugal terms, as well as from the damping of coactivated antagonist muscles. The model (3) was derived by assuming Coriolis and centrifugal effects to be negligible, and it is one of the purposes of this section to examine that assumption. Velocity-related terms arising from Coriolis and centrifugal terms are nonlinear and are unrelated to muscle coactivation. In order to determine whether these terms were larger than or comparable in size to the muscle-based terms, part of the model validation involved consideration of their simulated and actual contribution to the measured forces. The theta-based Coriolis and centrifugal forces may be written

$$C(\Theta_0, \dot{\Theta}) = B_J(\Theta_0)\dot{\Theta}\dot{\Theta}^T \tag{10}$$

TABLE II
AVERAGE FITTING ERRORS σ_1, σ_2 (N) FOR TWO HUMAN SUBJECTS

Subject	Position	Model (3)	(13)	(14)	(15)
1	1	0.21, 0.34	0.28, 0.53	0.28, 0.53	0.21, 0.35
	2	0.23, 0.56	0.28, 0.73	0.28, 0.73	0.23, 0.51
	3	0.33, 0.82	0.47, 0.99	0.47, 0.99	0.33, 0.84
	4	0.32, 0.45	0.37, 0.64	0.37, 0.64	0.32, 0.51
	5	0.27, 0.34	0.43, 0.53	0.43, 0.51	0.34, 0.42
2	1	0.36, 0.48	0.39, 0.54	0.38, 0.53	0.35, 0.48
	2	0.27, 0.66	0.29, 0.74	0.29, 0.73	0.27, 0.65
	3	0.41, 0.53	0.46, 0.58	0.45, 0.58	0.40, 0.55
	4	0.30, 0.50	0.36, 0.59	0.36, 0.58	0.31, 0.50
	5	0.40, 0.29	0.48, 0.42	0.48, 0.41	0.43, 0.32

where the matrix $B_J(\Theta_0)$ represents the joint-based squared- and coupled-velocity damping about the equilibrium position Θ_0, since the matrix $\dot{\Theta}\dot{\Theta}^T$ contains the terms $\dot{\theta}_i^2$ and $\dot{\theta}_i\dot{\theta}_j$. By using the relationship

$$\dot{X} = J(\Theta_0)\dot{\Theta} \tag{11}$$

and substituting functions of $\dot{X}_1$ and $\dot{X}_2$ for $\dot{\theta}_1$ and $\dot{\theta}_2$ in (10), $C(\Theta_0, \dot{\Theta})$ may be written in Cartesian variables as

$$C(\Theta_0, \dot{\Theta}) = B_C(\Theta_0)\dot{X}\dot{X}^T \tag{12}$$

where $B_C(\Theta_0)$ is a Cartesian squared- and coupled-velocity damping matrix.

Three alternative models were compared to (3) and to one another in terms of their fitting error. These models are:

$$F = M\ddot{X} + K(X - X_0) \tag{13}$$

$$F = M\ddot{X} + B_C\dot{X}\dot{X}^T + K(X - X_0) \tag{14}$$

$$F = M\ddot{X} + B[\dot{X}_1^2\dot{X}_2^2]^T + K(X - X_0) \tag{15}$$

where $X = [X_1 X_2]^T$ is the displacement vector. Model (13) neglects damping entirely, model (14) includes the Cartesian form of centrifugal and Coriolis forces, and model (15) modifies (3) by squaring the velocity terms, thereby rendering it nonlinear. These models were compared to the full linear model (3) on the basis of the average fitting error

$$\sigma = \frac{\sqrt{e^T e}}{N} \tag{16}$$

where e is a vector of fitting errors, or deviations from the measured force values, in the reconstructed or "fitted" version of the output, and N is the total number of data points. In the two-dimensional case considered, two displacement inputs were fitted independently to two different force outputs, yielding two independent σ-values for a given fitting, one for each output (σ_1 and σ_2). These average fitting errors were found at each test position for a parameter identification over the entire set of 16 perturbations.

Typical average fitting errors for two human subjects for models (3) and (13)–(15) are shown in Table II . The model (13), with no velocity-related terms, had higher error values than the linear model (3) in every case. In all but two of the twenty comparisons shown (two σ-values for each of five positions for two subjects), the difference was greater than or equal to 0.05 N, the dynamic noise figure for the force sensor. This indicates that velocity-related terms play a significant role and must be included in the identification.

Model (14), which considers Coriolis and centrifugal force-related velocity terms, had larger fitting errors than the linear model (3) in every case. In addition, the decrease in fitting error over model (13) was negligible, averaging less than 0.005 N. This result was confirmed in simulation by calculating the term $B_C\dot{X}\dot{X}^T$ in model (14) using the experimentally observed maximum arm endpoint velocity of 80 cm/s, and finding it to be one to two orders of magnitude smaller than the velocity-related $B\dot{X}$ term experimentally identified in model (3). Finally, the terms resulting from a first-order expansion and linearization about a median velocity of 40 cm/s of the velocity-related terms in (14), coupled with the maximum observed endpoint velocity, were found again to be one to two orders of magnitude too small to account for the experimentally identified terms. In summary, although velocity-related terms are significant in the identification, they do not arise from Coriolis or centrifugal forces, *i.e.,* from passive dynamic effects associated with the human arm's inertial and kinematic character.

Finally, fitting errors from model (15), which substituted a squared-velocity for the simple linear velocity term, were comparable to those from model (3). In twelve out of the twenty cases, the fitting error from model (3) was smaller, and in three out of these twelve cases, it was significantly smaller. In no case in which model (15) had a smaller fitting error was the difference greater than the sensor's dynamic noise figure.

In conclusion, the linear model (3) is the most applicable to the force-displacement relationship for the human arm endpoint in the face of small perturbations from an equilibrium point. Velocity-related terms are significant and are accounted for by neuromuscular effects, rather than by passive dynamic effects. The former include short-latency muscle spindle reflexes whose EMG latencies can be as short as 40 ms, resulting in small muscle force generation 50 ms after perturbation onset [16], as well as larger forces generated by longer-latency reflexes from both spindles and Golgi tendon reflexes. Houk has proposed specific models whereby these reflexes regulate muscle stiffness and viscoelastic effects [17], [18]. For the purposes of this paper, all of these effects are subsumed below the level of analysis of the model given by (3).

Relationship Between Joint Damping and Stiffness: The measured Cartesian matrices M, B, and K are related to the human arm joint impedance matrices I, B_Θ, and K_Θ, respectively, through the Jacobian $J(\Theta)$ as

$$I = J^T M J \tag{17a}$$

$$B_\Theta = J^T B J \tag{17b}$$

$$K_\Theta = J^T K J. \tag{17c}$$

The relationship between joint damping and stiffness has been investigated in the single-joint case for the human forearm and elbow joint [19]–[21], but not in the multi-joint case. In the single-joint case, Cannon and Zahalak [19] found the ratio τ between joint damping and stiffness to be nearly constant with a mean value of 0.05 s for muscle torques ranging from

TABLE III
SINGLE-CONSTANT JOINT DAMPING-STIFFNESS RELATIONSHIPS

	Assumption SS		Assumption SD	
Subject	$\tau(s)$	% error	ζ	% error
1	0.056±0.007	20	0.25±0.02	13
2	0.057±0.005	14	0.25±0.01	9
3	0.026±0.005	31	0.17±0.02	25
4	0.068±0.007	17	0.27±0.02	13
5	0.151±0.013	17	0.51±0.03	12
6	0.227±0.030	27	0.62±0.07	22
7	0.071±0.007	20	0.23±0.03	25
8	0.026±0.006	34	0.14±0.04	34
9	0.077±0.008	20	0.25±0.02	18
10	0.025±0.006	35	0.12±0.02	29
11	0.011±0.002	30	0.08±0.01	29

3.0 N-m to 30.0 N-m. In another set of experiments [20] involving varying levels of resistance to small pseudorandom perturbations, τ was found to increase from 0.058 s to 0.125 s in the transition from a "resist" to a "do not resist" task, and to decrease from 0.08 s to 0.025 s for the opposite transition. The damping ratio $\zeta = \sqrt{B^2/4KI}$, where B and K are the elbow damping and stiffness, respectively, and I is the forearm inertia, had a smaller percentage change in these transitions, increasing from 0.448 to 0.476 for the first, and decreasing from 0.338 to 0.218 for the second. Flash [10] noted that it was impossible on the basis of these experimental data to unequivocally determine the relationship between joint damping and stiffness. In the multi-joint case, the joint stiffness and damping matrices are of the form

$$R_\Theta = \begin{bmatrix} R_{11} & R_{12} \\ R_{21} & R_{22} \end{bmatrix} \tag{18}$$

where the term R_{11} is the net shoulder joint stiffness or damping, R_{22} is the net elbow joint stiffness or damping, and R_{12} and R_{21} are the doubly-connected joint parameters. We have demonstrated that both stiffness and damping have small percentage curl, so that R_{12} and R_{21} are approximately equal. This results in three joint parameters for both stiffness and damping. Flash [10] used two different assumptions about the relationship between these damping and stiffness parameters in order to estimate the joint damping values from the measured joint stiffnesses. These assumptions were based on the ambiguous data resulting from the single-joint experiments described above. The first was that the joint damping values scale simply with the stiffness values by a single constant τ, so that $B_{ij} = \tau K_{ij}$. The second was that the damping ratio ζ remains constant for all three viscous coefficients, so that $B_{ij} = 2\zeta\sqrt{I_{ij}K_{ij}}$, where I_{ij} is the i,j element of the inertia matrix. We shall refer to these assumptions as SS (single-constant scaling) and SD (single-constant damping ratio). The ability of these assumptions to explain the actual data was tested by least-squares fitting the calculated joint damping values and stiffnesses to the single constants τ and ζ for each subject. The results are shown in Table III, with a single standard deviation shown. The percentage error figure is the ratio of the average fitting error to the maximum value of the joint damping across all test positions for a given subject.

TABLE IV
MULTIPLE-CONSTANT JOINT DAMPING-STIFFNESS RELATIONSHIPS

	Assumption MS				Assumption MD			
Subject	τ_s	τ_e	τ_{tj}	% error	ζ_s	ζ_e	ζ_{tj}	% error
1	0.067	0.040	0.039	17	0.254	0.261	0.176	12
2	0.062	0.046	0.021	11	0.252	0.284	0.104	7
3	0.037	0.013	0.012	21	0.186	0.097	0.063	19
4	0.082	0.050	0.045	13	0.272	0.295	0.196	12
5	0.178	0.108	0.078	10	0.507	0.553	0.243	9
6	0.246	0.214	0.177	25	0.582	0.977	0.512	17
7	0.067	0.082	0.053	20	0.201	0.427	0.143	17
8	0.019	0.042	0.010	30	0.105	0.402	0.067	22
9	0.087	0.069	0.027	18	0.249	0.349	0.089	15
10	0.030	0.020	0.004	33	0.127	0.135	0.015	27
11	0.010	0.013	0.008	29	0.067	0.139	0.063	23

The scaling factor τ ranged from 0.011 s to 0.227 s, which was somewhat larger than the range of single-joint values (0.025 s to 0.125 s) previously found for the forearm [20]. The damping ratio ζ varied from 0.08 to 0.62, with a mean value of 0.26 and single standard deviation of 0.16, placing it within the range of mean values found in the single-joint case [20]. For nine out of the eleven subjects, assumption SD, which explicitly involved the joint inertias, yielded lower percentage error. Only one subject's data were better explained by the first assumption. In the Cartesian domain, this was reflected by the general deviation in orientation and shape of the damping ellipses from their corresponding stiffness ellipses. If the assumption SS of simple scaling between joint damping values and stiffnesses were valid, the eigenvectors of the joint and Cartesian stiffness matrices would be shared by their corresponding damping matrices, leading to identical shapes and orientations for damping and stiffness.

In order to examine the relative participation of shoulder, elbow, and two-joint impedances in both damping and stiffness, the above assumptions were modified to allow for an independent scaling constant and damping factor for each element of the joint impedance matrix. We shall refer to these assumptions as MS (multiple-constant scaling) and MD (multiple-constant damping ratio). For assumption MS, $B_{11} = \tau_s K_{11}$, $B_{22} = \tau_e K_{22}$, and $B_{12} = \tau_{tj} K_{12}$, where τ_s, τ_e, and τ_{tj} are scaling constants for the shoulder, elbow, and two-joint impedances, respectively. For assumption MD, $B_{11} = 2\zeta_s\sqrt{I_{11}K_{11}}$, $B_{22} = 2\zeta_e\sqrt{I_{22}K_{22}}$, and $B_{12} = 2\zeta_{tj}\sqrt{I_{12}K_{12}}$, where ζ_s, ζ_e, and ζ_{tj} are the damping ratios for the shoulder, elbow, and two-joint impedances, respectively. Table IV shows the results of fitting the data to these constants.

For assumption MS, the shoulder and elbow scaling constants τ_s and τ_e were larger than the two-joint constant τ_{tj} in every case. This implies that the relative participation of two-joint impedance is smaller for joint damping than for joint stiffness. This is reflected in a general trend for the Cartesian damping ellipses to be thinner than their stiffness counterparts. For assumption MD, the damping constant ζ is smallest for the two-joint impedance parameters in every case. Assumption MD, which included consideration of the joint inertia values, has smaller fitting error than assumption MS in every case.

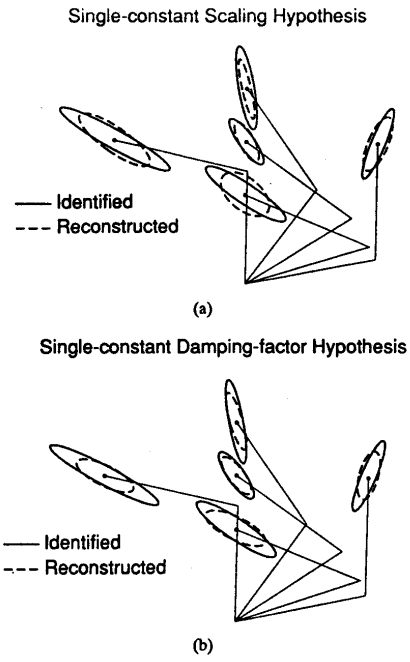

Fig. 8. Identified and reconstructed damping ellipses for the single-constant scaling (a) and damping-factor hypotheses (b), subject 1. In the majority of cases, the damping-factor hypothesis gives a better fit.

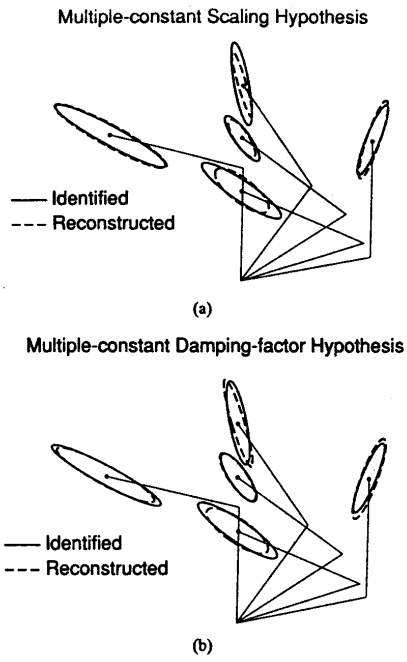

Fig. 9. Identified and reconstructed damping ellipses for the multiple-constant scaling and damping-factor hypotheses, subject 1.

The ability of the single- and multiple-constant assumptions to reconstruct the measured Cartesian damping ellipse was examined graphically, as well. Fig. 8 and 9 show the identified and reconstructed damping ellipses for the single- (SS and SD) and multiple-constant (MS and MD) assumptions, respectively, for a representative subject (subject 1). Assumption SD fits the actual data more closely than SS, especially at the proximal position. The MD and MS assumptions, however, are barely distinguishable.

In summary, the single-constant assumptions (SS and SD) do not capture the major features of the observed damping ellipses, although SD appears more likely than SS. The measured Cartesian damping ellipses generally have different orientations and shapes from their corresponding stiffness ellipses, which would not be the case if simple scaling (SS) were valid. The multiple-constant assumptions (MS and MD) are better able to reconstruct the observed damping ellipses, and MD results in somewhat smaller fitting error than MS. However, the differences between MS and MD in fitting error and in the ability to reconstruct the Cartesian damping ellipses may not be large enough to unequivocally prefer one over the other. Fitting according to assumption MS shows that the relative participation of two-joint muscles is smaller in damping than in stiffness, relative to the shoulder and elbow muscles. Fitting according to assumption MD shows lower damping factors for the two-joint muscles than for the elbow and shoulder muscles. The net effect of these general differences between shoulder/elbow muscles and two-joint muscles is to elongate the damping ellipses with respect to their corresponding stiffness ellipses.

IV. Postural Loaded Impedance

Because orientation was the most stable characteristic in the unloaded experiments, the potential for stiffness shape change was focused upon by taking data along the radial direction, i.e., at the proximal, reference, and distal positions. As before, the experimental data were fitted to (3). The state-variable filtering method was applied to the data, as before, and the stiffnesses were also determined by extracting the final static position and force values. The latter were found by scanning each trajectory backward in time starting with its final value, finding the first section of duration 0.2 s or more with velocity less than 5 mm/s, and averaging the force and displacement over this period.

Shifts in Equilibrium Point: In the unloaded experiment, the equilibrium position vector X_0 was expected to be near-zero, since each perturbation began with zero initial bias forces. This assumption was borne out by the data, the actual calculated equilibrium vectors being smaller than 1 mm in magnitude in every case. In the loaded experiment, X_0 was expected to be nonzero in those cases for which initial bias forces were nonzero, corresponding to a shift in the spring center. Actual and predicted equilibrium vectors were calculated for each of the four bias force directions at each position. The "actual" equilibrium vectors were those found

from the fitting of the data to the static equation

$$F_{\text{final}} = K_{\text{loaded}}(X_{\text{final}} - X_0) \tag{19}$$

where F_{final} and X_{final} are the final (static) force and displacement vectors, respectively, and K_{loaded} and X_0 are the implied loaded stiffness matrix and equilibrium vector, respectively. A static, rather than full dynamic, measurement of stiffness was used in this comparison in order to prevent skewing the results in favor of the equilibrium vectors implied by the initial bias forces. The predicted equilibrium vectors, on the other hand, were generated by averaging the initial and final unloaded stiffnesses to find an average unloaded stiffness K_{unloaded}, and calculating X_0 according to

$$X_0 = K_{\text{unloaded}}^{-1} F_{\text{bias}} \tag{20}$$

where F_{bias} is the bias force applied to the arm prior to each perturbation. The depicted predicted equilibrium vectors are thus based on the assumption that the loaded stiffnesses do not vary greatly from the unloaded stiffnesses. Fig. 10 compares the actual and predicted equilibrium position vectors for the proximal, reference, and distal positions for a single subject. The orientations of the actual equilibrium vectors correspond fairly closely to those predicted by the assumption that loaded and unloaded stiffnesses are equal to one another. Those differences in orientation and magnitude between the actual and predicted equilibrium vectors which appear are reflected in differences in size, shape, and orientation between the loaded and unloaded stiffnesses, which are discussed below.

The loaded stiffness characteristics have genuinely shifted spring centers, since the fitting errors for the loaded and unloaded cases are comparable in size. This was tested by using the final, static values of the force and displacement, and omitting the initial bias force, to avoid artificially reducing the average fitting error. Thus, in the face of perturbations superimposed upon a static bias force, the human arm responds as if displaced by some equilibrium vector X_0 from a "spring center" which does not correspond to its initial position. This extends the applicability of the hypothesis of human arm stiffness control to include the loaded case.

Impedance Modulation: In the loaded case, stiffness shapes at a given position varied by a factor between 1.1 and 1.5, and shapes were generally greater (i.e., more elongated) for bias forces along the ellipse major axes than for bias forces along the minor axes. Damping ellipse shapes varied by a factor between 1.1 and 1.5, but without a clear correspondence between shape changes and bias force directions. Stiffness size changes remained less than 50%, and there was no marked tendency for stiffness size to increase in the loaded case. This may have been partly due to the fact that the size of the bias forces had to be kept fairly small (approximately 1.0 N) in order for the resultant implied equilibrium vectors to be on the order of the perturbation sizes. Variations in stiffness orientation at a given position were smaller than 20 deg, and had no apparent relationship to the direction of bias force.

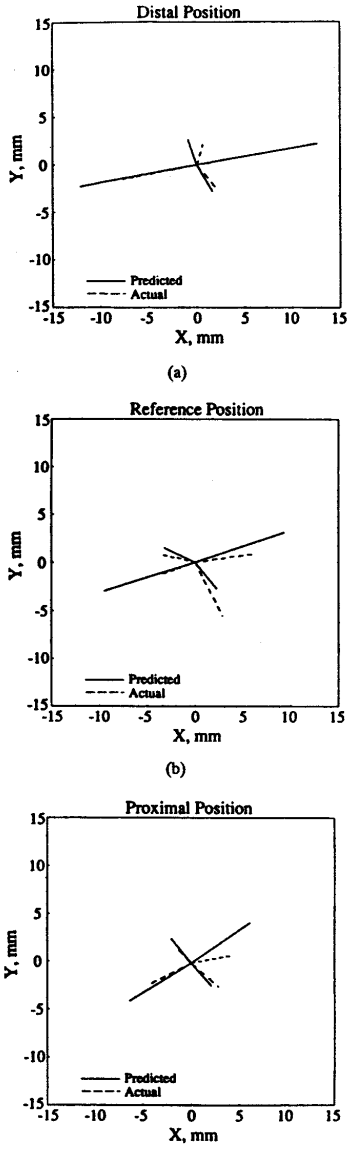

Fig. 10. Predicted and actual spring-center vectors in the face of preloading at the distal, proximal, and reference positions. The spring centers shift in the expected directions, with some variations in magnitude and orientation.

V. Conclusion

This paper extends the characterization of human arm impedance control beyond the measurement of unloaded postural stiffness. Three research themes have been pursued: measurement of the dynamic components of postural impedance (mass and damping), investigation of the relationship between these components and postural stiffness, and characterization of postural stiffness modulation under various cognitive conditions and in the face of initial static loading.

The results of the research have lead to an improved understanding of human arm control modalities. The mass and

damping components of impedance were found, like the stiffness component, to have small rotational components. Doubly joint-connected muscles were found to play a relatively smaller role in damping than in stiffness, causing damping ellipses to be more strongly directional thoughout the human arm workspace than their stiffness counterparts. In the case of stiffness modulation in response to cognitive cues, the basic strategy for increasing stiffness along a given direction was to increase it in all directions (*i.e.*, increase stiffness size, rather than significantly altering stiffness shape or orientation.) The significance of this is that the three basic arm muscle groups, shoulder, elbow, and two-joint, tend to work in concert with one another in increasing stiffness, rather than exhibiting a large degree of independence. By applying initial static bias forces to the arm endpoint and observing regular shifts in the arm's spring center, or equilibrium position, the validity of the impedance control hypothesis in the loaded postural case was confirmed.

The full characterization of human arm endpoint impedance is potentially applicable to the design and configuration of a wide variety of human-machine and human-object interaction tasks. There are many such tasks in which the human arm traverses its workspace, as opposed to fine-motion tasks in which hand and finger motions are of primary importance. In the area of teleoperation, where force reflection is sometimes used to give the operator greater dexterity and a richer sense of the environment with which the controlled manipulator is interacting, the results of human arm impedance measurement could be used in several ways. Human impedance characteristics could be "mapped" onto the slave telemanipulator by operating it under (robotic) impedance control [22] with the desired input trajectory specified by human guidance of the master manipulator, causing the resulting contact dynamics of the slave with its environment to resemble those of the human arm. Reflected forces could be simply those experienced by the slave, or could be transformed based on knowledge of the current configuration of the human arm and its corresponding impedance. For example, forces in directions of larger stiffness could be amplified relative to those of smaller stiffness in order to give the human more uniform sensitivity to environmental forces. In the area of prosthetics, where restoration of natural limb function by imitation of the intact human arm is an area of research [5], knowledge of the damping characteristic gives a richer description of the mechanical behavior of the human arm than that afforded by stiffness alone. Integration of the results of full impedance measurement of the human arm with research characterizing the intent of neuromuscular commands to the arm could lead to the design of artificial limbs that more closely mimic their intact counterparts.

APPENDIX
CARTESIAN MODEL OF HUMAN ARM ENDPOINT

Fig. 1 shows a simplified two-link model of the human arm in the horizontal plane [8], in which the numerous muscles present in the arm are brought together into three basic groups: 1) singly joint-connected shoulder muscles (SS), 2) singly joint-connected elbow muscles (SE), and 3) doubly joint-connected shoulder-elbow muscles (DJ). Each of the muscle elements in Fig. 1 is a linear series combination of a springlike and a viscous damping element. For small excursions from an equilibrium theta position Θ_0, a linear model of the torque-displacement relationship is

$$\tau = K_{\Theta_0}[\Theta - \Theta_0] + B_{\Theta_0}\dot{\Theta} \tag{21}$$

where

$$K_{\Theta_0} = \begin{bmatrix} K_s + K_d & K_d \\ K_d & K_e + K_d \end{bmatrix} = \begin{bmatrix} K_{11} & K_{12} \\ K_{21} & K_{22} \end{bmatrix}$$
$$B_{\Theta_0} = \begin{bmatrix} B_s + B_d & B_d \\ B_d & B_e + B_d \end{bmatrix} = \begin{bmatrix} B_{11} & B_{12} \\ B_{21} & B_{22} \end{bmatrix}$$

where K_{Θ_0} and B_{Θ_0} are the joint stiffness and damping matrix, respectively, at the equilibrium position Θ_0, and the subscripts s, e, and d designate the impedances due to the shoulder, elbow, and doubly-connected muscle groups, respectively. The inertia matrix $I(\Theta_0)$ and Coriolis and centrifugal effects $C(\Theta_0, \dot{\Theta})$ associated with the arm may be approximated by modeling the two links as uniform cylinders. The full joint-based human arm model then becomes

$$\tau = I(\Theta_0)\ddot{\Theta} + C(\Theta_0, \dot{\Theta}) + B_{\Theta_0}\dot{\Theta} + K_{\Theta_0}[\Theta - \Theta_0]. \tag{22}$$

In order to relate the joint-based model to its Cartesian counterpart, we use the relationship

$$\tau = J^T(\Theta_0)F \tag{23}$$
$$\delta X = J(\Theta_0)\delta\Theta \tag{24}$$
$$\dot{X} = J(\Theta_0)\dot{\Theta} \tag{25}$$

where F is the Cartesian force applied to the endpoint of the arm. (24) is exact only for infinitesimal displacements, but is approximately valid for small excursions from the equilibrium point, so that

$$X - X_0 \approx J(\Theta_0)[\Theta - \Theta_0]. \tag{26}$$

Differentiating (25), we obtain

$$\ddot{X} = J(\Theta_0)\ddot{\Theta} + \dot{J}(\Theta_0)\dot{\Theta}. \tag{27}$$

The time rate of change of the Jacobian is negligible for small excursions, so we make the approximation

$$\ddot{X} \approx J(\Theta_0)\ddot{\Theta}. \tag{28}$$

Using the kinematic relationships (23), (25), (26), and (28) in (22), neglecting Coriolis and centrifugal forces, dropping

theta-arguments for simplicity, and rearranging, we obtain

$$F = J^{-T}\{IJ^{-1}\ddot{X} + B_{\Theta_0}J^{-1}\dot{X} + K_{\Theta_0}J^{-1}[X - X_0]\}. \quad (29)$$

Consolidating terms, we may finally write

$$F = M\ddot{X} + B\dot{X} + K(X - X_0) \quad (30)$$

where the Cartesian mass, damping, and stiffness matrices at the equilibrium position X_0 are

$$M = J^{-T}IJ^{-1} \quad (31a)$$

$$B = J^{-T}B_{\Theta_0}J^{-1} \quad (31b)$$

$$K = J^{-T}K_{\Theta_0}J^{-1}. \quad (31c)$$

REFERENCES

[1] R. B. Stein, "What muscle variable(s) does the nervous system control in limb movements?" *The Behavioral and Brain Sciences*, vol. 5, pp. 535–577, 1982.

[2] A. G. Feldman , "Change in the length of the muscle as a consequence of a shift in equilibrium in the muscle-load system," *Biophys.*, vol. 19, pp. 544–548, 1974.

[3] E. Bizzi, N. Accornero, W. Chapple, and N. Hogan, "Arm trajectory formation in monkeys," *Exp. Brain Research*, no. 40, pp. 139–143, 1982.

[4] J. A. S. Kelso, and K. G. Holt, "Exploring a vibratory systems analysis of human movement production," *J. Neurophys.*, no. 43, pp. 1183–1196, 1980.

[5] N. Hogan, "Mechanical impedance control in assistive devices and manipulators," in *Proc. Joint Automatic Contr. Conf.*, Aug 1980.

[6] T. R. Nichols and J. C. Houk, "The Improvement in linearity and the regulation of stiffness that results from the actions of the stretch reflex," *J. of Neurophysiology*, no. 39, pp. 119–142, 1976.

[7] N. Hogan, "The mechanics of multi-joint posture and movement," *Biological Cybern.*, no. 52, pp. 315–331, 1985.

[8] N. Hogan, "Adaptive control of mechanical impedance by coactivation of antagonist muscles," *IEEE Trans. Automat. Contr.*, vol. 29, no. 8, pp. 681–690, 1984.

[9] F. A. Mussa-Ivaldi, N. Hogan, and E. Bizzi, "Neural, mechanical, and geometric factors subserving arm posture in humans," *J. Neurosci.*, vol. 5, no. 10, pp. 2732–2743, 1985.

[10] T. Flash, "The control of hand equilibrium trajectories in multi-joint arm movements," *Biological Cybern.*, vol. 57, pp. 257–274, 1987.

[11] J. M. Dolan, *An Investigation of Postural and Voluntary Human Arm Impedance Control*, Ph.D. dissertation, Carnegie Mellon Univ., Aug 1991.

[12] J. M. Dolan, M. B. Friedman, and M. L. Nagurka, "A testbed for measurement of human arm impedance parameters," in *Proc. IEEE Conf. Syst. Eng.*, Pittsburgh, PA, Aug 1990, pp. 123–126.

[13] J. C. Pezzack, R. W. Norman, and D. A. Winter, "An assessment of derivative determining techniques used for motion analysis," *J. Biomechanics*, pp. 377–382, 1977.

[14] H. Hatze, "An algorithm for computing higher-order derivatives of noisy experimental data sequences," Tech. rep. TWISK 123, Nat. Res. Inst. Math. Sci., Nov 1979.

[15] T. C. Hsia, *System Identification*. Lexington, MA: D. C. Heath, 1977.

[16] J. H. J. Allum, K.-H. Mauritz, and H. Voegele, "The mechanical effectiveness of short latency reflexes in human triceps surae muscles revealed by ischaemia and vibration", *Exp. Brain Res.*, no. 48, pp. 153–156, 1982.

[17] J. C. Houk, "Regulation of stiffness by skeletomotor reflexes", *Ann. Rev. Physiol.*, no. 41, pp. 99–114, 1979.

[18] C. C. A. M. Gielen and J. C. Houk, "Nonlinear viscosity of human wrist", *J. Neurophys.*, vol. 52, no. 3, pp. 553–569, 1984.

[19] S. Cannon, and G. I. Zahalak, "The mechanical behavior of active human skeletal muscle in small oscillations," *J. Biomechanics*, vol. 15, pp. 111–121, 1982.

[20] F. Lacquaniti, F. Licata, and J. F. Soechting, "The mechanical behavior of the human forearm in response to transient perturbations", *Biological Cybern.*, no. 44, pp. 35–46, 1982.

[21] W. A. MacKay, D. J. Crammond, H. C. Kwan, and J. T. Murphy, "Measurements of human forearm viscoelasticity", *J. Biomechanics*, no. 19, pp. 231–238, 1986.

[22] N. Hogan, "Impedance control: An approach to manipulation: Part I—Theory," *ASME J. Dyn. Syst., Measurement, Contr.*, pp. 1–7, Mar. 1985.

John Dolan (M'83) received the B.S.E. degree in mechanical engineering from Princeton University in 1980, and the M.E. and Ph.D. degrees in mechanical engineering from Carnegie Mellon University, Pittsburgh, in 1987 and 1991, respectively.

He is currently a project scientist at The Robotics Institute and the Engineering Design Research Center, Carnegie Mellon University. From 1980 through 1981 he was a research associate at the German Research and Testing Facility for Aerospace Technology (DFVLR). From 1981 through 1985 he served in the U.S. Army, working on the application of artificial intelligence to military intelligence problems. His research interests include robotic control, biomechanics, and man–machine interaction. He held a Fulbright scholarship at the Technical University of Munich from 1980 through 1981.

Dr. Dolan was elected to the Sigma Xi and Tau Peta Pi engineering honor societies.

Mark Friedman received the B.S. degree in biology in 1966 from Massachusetts Institute Technology, Cambridge, and the Ph.D. degree in neurobiology in 1972 from Rutgers University. From 1972 through 1974 he was a University Fellow doing post-doctoral research at the University of Edinburgh, Scotland. In 1974 he joined the psychology faculty of Carnegie Mellon University. After developing an interest in rehabilitative technology through volunteer work, he became a Research Engineer at CMU's Robotics Institute in 1980. With several of his students, Dr. Friedman co-founded Sentient Systems Technology, Inc. to commercialize technology conceived in the Technical Volunteer Program at The Rehabilitation Institute of Pittsburgh. This company has become the leading producer of eye–gaze controlled computers and one of the leaders for augmentative communication devices. In 1990, Dr. Friedman formed a consulting engineering company, AugmenTech, Inc., which does work in cognitive prosthetics. He teaches as an Adjunct Professor in CMU's Biomedical Engineering Program.

Mark Nagurka (M'86) received the B.S. and M.S. degrees in mechanical engineering and applied mechanics, in 1978 and 1979, respectively, from the University of Pennsylvania, Philadelphia, PA, and the Ph.D. degree in mechanical engineering in 1983 from the Massachusetts Institute of Technology, Cambridge.

Following graduation, he joined Carnegie Mellon University where he is currently an Associate Professor of Mechanical Engineering and an affiliated member of The Robotics Institute and the Biomedical Engineering Program. His research work focuses on the development and integration of control methods into practical mechanical systems, and is applied to projects in precision engineering and biomechanics. Two areas of special interest are parameterization methods for solving optimal control problems, and gain domain tools for control system analysis and design. He is currently serving as a Technical Editor of ASME Applied Mechanics Review and a Technical Associate Editor of IEEE CONTROL SYSTEMS MAGAZINE.

Dr. Nagurka is a registered Professional Engineer in the Commonwealth of Pennsylvania, and is active in several engineering societies, including ASEE and ASME.